Ultrasonics Sonochemistry 75 (2021) 105608

Contents lists available at ScienceDirect

Ultrasonics Sonochemistry

journal homepage: www.elsevier.com/locate/ultson

Predicting initial nucleation events occurred in a metastable nanodroplet during acoustic droplet vaporization

Dui Qin *, Qingqin Zou, Shuang Lei, Wei Wang, Zhangyong Li *

Chongqing Engineering Research Center of Medical Electronics and Information Technology, Department of Biomedical Engineering, School of Bioinformatics, Chongqing University of Posts and Telecommunications, Chongqing 400065, PR China

ARTICLE INFO

Keywords:
Acoustic droplet vaporization
Bubble nucleation
Phase-change nanodroplets
Thermodynamics

ABSTRACT

Acoustic droplet vaporization (ADV) capable of converting liquid perfluorocarbon (PFC) micro/nanodroplets into gaseous microbubbles has gained much attention due to its medical potentials. However, its physical mechanisms for nanodroplets have not been well understood due to the disappeared superharmonic focusing effect and the prominent Laplace pressure compared to microdroplets, especially for the initial ADV nucleation occurring in a metastable PFC nanodroplet. The classical nucleation theory (CNT) was modified to describe the ADV nucleation *via* combining the phase-change thermodynamics of perfluoropentane (PFP) and the Laplace pressure effect on PFP nanodroplets. The thermodynamics was exactly predicted by the Redlich–Kwong equation of state (EoS) rather than the van der Waals EoS, based on which the surface tension of the vapor nucleus as a crucial parameter in the CNT was successfully obtained to modify the CNT. Compared to the CNT, the modified CNT eliminated the intrinsic limitations of the CNT, and it predicted a larger nucleation rate and a lower ADV nucleation threshold, which agree much better with experimental results. Furthermore, it indicated that the nanodroplet properties exert very strong influences on the nucleation threshold instead of the acoustic parameters, providing a potential strategy with an appropriate droplet design to reduce the ADV nucleation threshold. This study may contribute to further understanding the ADV mechanism for PFC nanodroplets and promoting its potential theranostic applications in clinical practice.

1. Introduction

Phase-change nanodroplets emerging as an alternative to conventional microbubbles are highly attractive for cancer theranostics. They are usually composed of a volatile perfluorocarbon (PFC) liquid core and a stabilizing shell of lipid, polymer, protein, or fluorinated surfactant [1–4]. Thanks to their smaller size and longer circulation time *in vivo* relative to microbubbles, the PFC nanodroplets are able to passively accumulate in solid tumors *via* the enhanced permeability and retention (EPR) effect [5]. Upon external ultrasound stimulation above a certain threshold, these nanodroplets can be vaporized into microbubbles *in situ*, a process known as acoustic droplet vaporization (ADV) [1–4]. It can significantly enhance the ultrasound imaging in the tumor region for treatment guidance/monitoring [6,7], meanwhile, can also perform therapeutic actions such as on-demand drug release [8,9], cell sonoporation [10,11], HIFU sensitization [12,13], and targeted neuromodulation [14], etc. For these theranostic applications, the PFC nanodroplets are expected to be reliable and effective only if they do not spontaneously vaporize or dissolve after intravenous injection *in vivo*, and also can be vaporized *in situ* with a low enough threshold to avoid adverse effects, hence requiring a trade-off between *in vivo* stability and ADV threshold [2,4].

It is challenging to achieve an optimal balance between *in vivo* stability and ADV threshold due to the discrepancy of high stability and low ADV threshold, as well as the complex effects of various parameters, such as nanodroplet properties (e.g., PFC core species, shell composition and droplet size), acoustic parameters (e.g., ultrasound frequency and pulse duration), medium rheology and ambient pressure/temperature, etc. [15–19]. One attempt has been made to reduce the ADV threshold *via* utilizing PFC species with lower boiling points (e.g., perfluoropropane or perfluorobutane) [20,21], but these PFCs are more water soluble [22], faster clear and more likely to occur spontaneous vaporization during *in vivo* circulation [1–4], which would limit their utility. Alternatively, replacing them with perfluoropentane (PFP) having a relatively higher boiling point and lower solubility should notably increase the circulation persistence, but the latter is more difficult to

* Corresponding authors at: No. 2 Chongwen Road, Nan'an District, Chongqing 400065, PR China.
E-mail addresses: duiqin@cqupt.edu.cn (D. Qin), lizy@cqupt.edu.cn (Z. Li).

https://doi.org/10.1016/j.ultsonch.2021.105608
Received 24 April 2021; Received in revised form 16 May 2021; Accepted 21 May 2021
Available online 25 May 2021

vaporize because of a higher ADV threshold [1–4]. Droplet vaporization is a thermodynamic phenomenon. The equilibrium phase-change thermodynamics of perfluoropropane and perfluorobutane have been described by the simplest cubic equation of state (EoS), i.e., van der Waals (vdW) EoS [23]. It can give a qualitative prediction of phase equilibrium, but there is generally a vast difference as compared with the experimental values [24]. Moreover, for now, there has been little research on the phase-change thermodynamics of the PFP that has a relatively higher *in vivo* stability while requiring a higher ADV threshold. Thus, understanding the phase-change thermodynamics of different PFC species and the physical mechanisms driving ADV is of great importance for optimal application of ADV in theranostics.

Numerous experiments have been carried out to investigate the ADV process and determine the ADV threshold, nevertheless, it exhibited a large difference among them, probably due to the experimental inconsistencies and the sensitivity of ADV threshold to multiple parameters [15–19]. Alternatively, theoretical prediction of ADV threshold has also been performed *via* investigating bubble growth in the PFC droplet [25–28]. However, note that a small vapor bubble nucleus was assumed to be existed prior to the bubble growth, and it has demonstrated that the bubble growth and the predicted ADV threshold strongly depend on the initial radius of the bubble nucleus [25,28]. The formation of the initial vapor bubble nucleus (i.e., bubble nucleation) is a prerequisite for ADV and it also needs a threshold, so that the ADV threshold is co-determined by the thresholds of initial bubble nucleation and subsequent bubble growth. To date, less attention has been paid to the initial ADV nucleation in a PFC nanodroplet, because it can hardly be detected experimentally even using a microscopic imaging system with a high-resolution and high-speed camera. Therefore, numerical investigation of the initial bubble nucleation events occurred in a PFC nanodroplet, taking the phase-change thermodynamics of PFC liquids into account, is essential for subsequent bubble growth and ultimate ADV threshold prediction.

During ADV process, bubble nucleation could occur by heterogeneous nucleation originating on the pre-existing interfaces or imperfection [29], or by homogeneous nucleation in the pure liquid phase devoid of such interfaces [23,30]. Classical nucleation theory (CNT), the most commonly-used theory of nucleation, has been used to predict the ADV threshold of PFP microdroplets *via* homogeneous or heterogeneous nucleation [23,29,30]. Especially, Miles et al. first combined the CNT with the superharmonic focusing effect of the microdroplets to predict the ADV nucleation threshold of PFP microdroplets [30], but this mechanism may disappear for small droplets of 2 μm or less [28]. Moreover, compared to the PFP microdroplet, the nanodroplet always experiences a much larger Laplace pressure and significantly elevates the liquid pressure in the nanodroplet, resulting in a greater impact on the initial ADV nucleation that occurs in the pressurized PFP core [23]. More research is necessary to understand the ADV mechanism for nanodroplets. More importantly, the CNT is usually criticized for assuming the surface tension of critical bubble σ_r equal to the macroscopic surface tension of flat interface σ_∞, also known as the "capillarity approximation'' [31]. Consequently, it leads to large errors in the nucleation rate at a higher degree of metastability, and fails to predict the loss of stability at the spinodal. These intrinsic limitations have caused an obvious overestimation of nucleation threshold [32,33]. Therefore, accurately estimating the σ_r with experimentally controllable parameters is crucial to overcome the current limitations. It has demonstrated that the σ_r can be expressed as a function of the experimentally controlled overpressure of liquid phase, which depends on the actual liquid pressure and temperature as well as the phase-change thermodynamics of the liquid [34–36].

In this study, a modified CNT with the σ_r rather than the σ_∞ was developed to predict the ADV nucleation threshold of nanodroplets *via* combining the phase-change thermodynamics of PFP and the Laplace pressure effect on PFP nanodroplets. The thermodynamics over a wide range of pressures and temperatures in the liquid state, the metastable state and the vapor state was predicted by different EoS, and the superior one was chosen compared to experimental results. Furthermore, the effects of droplet properties and acoustic parameters on the ADV nucleation threshold were examined.

2. Theory and methods

The schematic diagram of the ADV nucleation occurring in a PFP nanodroplet is illustrated by Fig. 1. Upon ultrasound stimulation, a spherical vapor bubble nucleus with radius r^* and surface tension σ_r is formed by spontaneous fluctuations in the metastable PFP nanodroplet immersed in ambient water, which has a droplet radius of R_d and a surface tension of σ_{dw} at the droplet-water interface. The ADV nucleation is assumed to occur by the homogeneous nucleation at the ultrasound phase where acoustic pressure values $P_a(t)$ are the lowest and remain reasonably constant, and it is accurately described by the modified CNT.

2.1. Phase-change thermodynamics of PFP

The phase-change thermodynamics of PFP from liquid to vapor is estimated by the classic cubic EoS, presenting an algebraic relation between pressure (P), molar volume (V) and temperature (T). They have been widely used due to their reliability and simple form, which can in general be represented as [37]

$$P = \frac{RT}{V-b} - \frac{a\alpha(T)(V-\eta)}{(V-b)\left(V^2+\delta V+\varepsilon\right)}, \tag{1}$$

where R is the universal gas constant, the parameters a and b are evaluated as [37]

$$a = \frac{\Omega_a R^2 T_c^2}{P_c}, b = \frac{\Omega_b R T_c}{P_c}. \tag{2}$$

The equation-dependent parameters $\alpha(T)$, η, δ and ε, as well as the constants Ω_a and Ω_b are given in Table 1. Note that the Eq. (1) only needs two universal properties of the PFP liquid, i.e., the critical temperature (T_c = 420.55 K) and critical pressure (P_c = 2.045 MPa), which are obtained from the National Institute of Standards and Technology (NIST, USA) data [38].

2.2. Local pressure description in PFP nanodroplets

As shown in Fig. 1, for a spherical PFP nanodroplet, the local liquid pressure P_l in the nanodroplet when subjected to ultrasound stimulation is determined by

$$P_l = P_\infty + P_{Lap} + P_a(t), \tag{3}$$

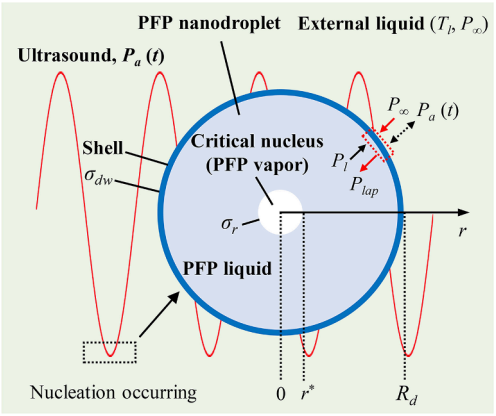

Fig. 1. Schematic diagram for modeling initial bubble nucleation in a perfluoropentane (PFP) nanodroplet during acoustic droplet vaporization (ADV).

Table 1
Parameters and functions of cubic equation of state (EoS).

EoS	$\alpha(T)$	η	δ	ε	Ω_a	Ω_b
vdW	1	b	0	0	0.421875	0.125
RK	$1/\sqrt{T_r}$	b	b	0	0.42748	0.08664

Abbreviations of EoS: van der Waals (vdW) and Redlich–Kwong (RK).
$T_r = T/T_c$ is the reduced temperature, where T_c is the critical temperature of PFP.

where P_∞, P_{Lap} and P_a are the ambient pressure, Laplace pressure and applied acoustic pressure, respectively. The acoustic pressure P_a is given by $P_a = P_A sin(2\pi ft)$, where P_A is the ultrasound amplitude and f is the ultrasound frequency.

The Laplace pressure P_{Lap} experienced by a PFP nanodroplet is given by

$$P_{Lap} = \frac{2\sigma_{dw}}{R_d}. \tag{4}$$

The Laplace pressure is determined by the radius of the PFP nanodroplet R_d and the surface tension at the droplet-water interface σ_{dw}. The surface tension is dependent on the droplet shell composition, such as surfactants, proteins, lipids and polymers that exhibit a variety of surface tension values [2].

2.3. A modified CNT for ADV nucleation in a PFP nanodroplet

The occurrence of ADV nucleation in a PFP nanodroplet means that a vapor bubble nucleus is formed through spontaneous fluctuations in pure PFP liquid, which has been moved from a stable liquid state to a metastable liquid state by a decrease in pressure. Nucleation is an activated process, in which an energy barrier must be surmounted to transform the metastable liquid phase to the stable vapor phase. The work W required for the formation of a vapor bubble nucleus with a radius r in the metastable liquid is given by [33]

$$W(r) = 4\pi r^2\sigma + \frac{4\pi r^3}{3}(P_l - P_v) + N(\mu_v - \mu_l), \tag{5}$$

where σ is the surface tension at the PFC liquid–vapor interface, P_v is the vapor pressure in a newly formed vapor bubble nucleus, N is the number of molecules inside the bubble nucleus, μ_v and μ_l are the chemical potentials of the gas phase and the liquid phase, respectively.

It is well-known that the work W exhibits a maximum W^* at the critical bubble radius r^* given by $\partial W/\partial r|_{r=r^*} = 0$, where superscript * denotes conditions at the critical size [33]. The probability of growth is greater than the probability of shrinking for vapor bubble nuclei whose radii are greater than the critical radius, whereas the probability of shrinking prevails for smaller bubble nuclei. For a critical bubble nucleus, the probability of shrinking is equal to that of growth, which implies chemical equilibrium ($\mu_v^* = \mu_l^*$) in the condition of $r = r^*$. The critical size can be obtained by applying these conditions to Eq. (5), resulting in a Young-Laplace-type equation:

$$r^* = \frac{2\sigma}{P_v - P_l}. \tag{6}$$

Note that the surface tension σ is usually approximated to the macroscopic surface tension of flat interface σ_∞ in the CNT. To overcome the intrinsic limitations of the CNT caused by this "capillarity approximation", the accurate surface tension of the critical nucleus σ_r as a function of the experimentally controllable scaled overpressure of liquid phase ξ is given by [34,35]

$$\sigma_r(\xi) = \sigma_\infty(T_l)\phi(\xi)^{1/3}$$

where $\phi(\xi) = (1-\xi)(1+0.5\xi)^2$. The ξ is determined by the actual liquid pressure P_l and temperature T_l as well as the phase-change thermodynamics of the PFP. At the same temperature, the ξ is given by [35,36]

$$\xi = \frac{\Delta P}{\Delta P_s} = \frac{P_{sat}(T_l) - P_l(T_l)}{P_{sat}(T_l) - P_{spin}(T_l)}$$

where P_{sat} and P_{spin} are the saturation vapor pressure and spinodal pressure, respectively. The variable overpressure ΔP is experimentally controlled *via* the actual pressure and temperature of the metastable liquid. It is a measure of the degree of liquid metastability, ranging from $\Delta P = 0$ at the binodal ($\xi = 0$) to $\Delta P = \Delta P_s$ at the spinodal ($\xi = 1$). Thus, the CNT is modified as

$$r^*(T_l, P_l) = \frac{2\sigma_r(T_l, P_l)}{P_v(T_l, P_l) - P_l}, \tag{9}$$

$$W^*(T_l, P_l) = \frac{16\pi\sigma_r(T_l, P_l)^3}{3[P_v(T_l, P_l) - P_l]^2}, \tag{10}$$

$$J(T_l, P_l) = J_0 exp\{\frac{-16\pi\sigma_r(T_l, P_l)^3}{3k_B T_l[P_v(T_l, P_l) - P_l]^2}\}, \tag{11}$$

where W^* is the critical work required to form the critical vapor bubble nucleus, J is the nucleation rate that denotes the number of critical nuclei formed per unit time and volume, $J_0 = \sqrt{3\sigma_r(T_l, P_l)\rho_l^2/\pi m^3}$ is the pre-exponential factor, ρ_l is the liquid density, m is the mass of single molecule, k_B is the Boltzmann constant. Furthermore, a correction between the vapor pressure inside the vapor bubble nucleus P_v and the saturation pressure P_{sat} is introduced as follows [39]:

$$P_v(T_l, P_l) = P_{sat}(T_l) exp(-\frac{P_{sat}(T_l) - P_l}{\rho_l R T_l}). \tag{12}$$

2.4. ADV nucleation thresholds

In the CNT, for a sample of volume V, the probability of bubble nucleation Σ within a time τ is [40]

$$\Sigma = 1 - exp(-JV\tau), \tag{13}$$

where V represents the nanodroplet volume, τ is modelled as a fraction of the ultrasound wave where acoustic pressure values are the lowest and remain reasonably constant. Thus, τ is approximated as $1/10f$ to ensure that P_l variations within this time interval are negligible, similar to that used previously [33]. The ADV nucleation threshold P_{th} is defined as the absolute value of the acoustic pressure P_a at which Σ reaches 50%, thus the P_{th} is given by

$$P_{th} = |P_a| = P_v - P_\infty - P_{Lap} - \left[\frac{16\pi\sigma_r^3}{3k_B T_l ln(J_0 V\tau/ln2)}\right]^{1/2}. \tag{14}$$

It is worth noting that the τ appears within the logarithm in Eq. (14), and so, the ADV nucleation threshold P_{th} would has a weak dependence on τ.

2.5. Computational conditions

Unless otherwise indicated, we consider ADV of PFP nanodroplets in water at $P_\infty = 1$ atm and $T_l = 310$ K, as depicted in Fig. 1. The applied ultrasound frequency f is 6 MHz, pulse duration τ_p is 16.7 μs (i.e., 100 cycles per pulse), pulse-repetition frequency is 10 Hz and total irradiation time is 10 s, referring to the experimental condition used in previous experiments [18].

The temperature-dependent properties of PFP liquid (σ_∞ and ρ_l) were obtained from NIST data [38], and corresponding expressions as a function of temperature were further found by fitting with the NIST data. An appropriate asymptotic relation for the temperature-dependent

surface tension is used [41]

$$\sigma_\infty(T_l) = A(1 - T_l/T_c)^{2\upsilon}, \tag{15}$$

where A is the coefficient and υ is the critical exponent that describes the behavior of the surface tension as approaching the critical point. The values obtained for the coefficients in Eq. (15) were $A = 0.0425$ and $\upsilon = 0.6$ with a root mean square deviation (RMSD) of 3.66×10^{-6}. For the temperature-dependent liquid density, a power series of the type is given by [42]

$$\rho_l = \rho_c[1 + \sum_{i=1}^{6} B_i(1 - T_l/T_c)^{i/3}] \tag{16}$$

where $\rho_c = 759.53$ kg·m^{-3} is the critical density of PFP liquid. The values for constants B_i were given by $B_1 = -0.4245$, $B_2 = 8.919$; $B_3 = -17.61$, $B_4 = 19.63$, $B_5 = -10.92$ and $B_6 = 2.655$ with a RMSD of 0.077. As shown in Fig. 2, it demonstrated that the obtained expressions exhibit a great representation of the surface tension and the liquid density over a wide temperature range from 280 K to 420 K.

3. Results and discussion

3.1. Phase-change thermodynamics of PFP

By solving the cubic EoS shown in Eqs. (1) and (2) with the parameters given in the Table I, one can derive the pressure–volume isotherms of the PFP for different temperatures, as illustrated in Fig. 3(a). For one isotherm, there is an isobaric line that represents equilibrium between the gas phase and liquid phase as displayed by the dotted line in Fig. 3 (b). It means that the areas above and below the isobaric line must be equal, i.e., the area of region 1 is equal to the area of region 2. This is the so-called Maxwell's construction [43]. The intersection points of the isobaric line and isotherm (points A and D) are known as the binodal points. For one temperature below the critical temperature, local minimum and maximum are found on the isotherm, which represent the liquid spinodal point (point B) and vapor spinodal point (point C), respectively. Using these methods, the binodal curve (saturation curve) and spinodal curve can be constructed as shown in Fig. 3(c). Finally, a pressure–volume phase diagram of the PFP was constructed, as displayed in Fig. 3(d). The PFP can be in the liquid phase, in the vapor phase, in the liquid–vapor coexistence phase, at liquid–vapor equilibrium (binodal curve), at the spinodal curve, or in the metastable (superheated or supercooled) domains.

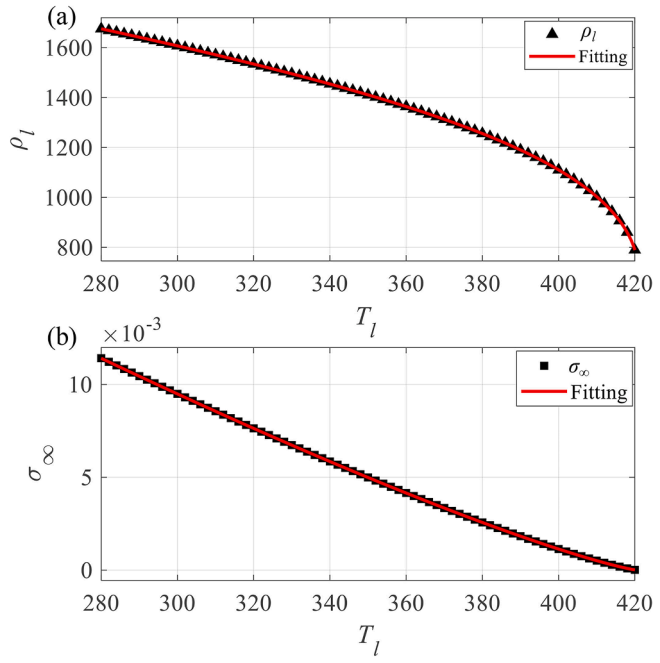

Fig. 2. (a) The surface tension at the PFP liquid–vapor interface and (b) the density of PFP liquid as a function of temperature. The points represent the data obtained from NIST date and the lines represent the fitting results of Eqs. (15) and (16), respectively.

According to the calculation procedures shown in Fig. 3, the pressure–temperature phase diagram of the PFP derived from the vdW and Redlich–Kwong (RK) EoS was presented in Fig. 4(a). The dashed and solid curves as a function of temperature are the binodal curves and spinodal curves for vdW (blue) and RK EoS (red), respectively. The binodal curve is the liquid–vapor coexistence or the saturation curve of PFP, while the spinodal curve represents its thermodynamic stability limit. The extremum of the binodal curve coincides with the one of the spinodal curve and it is known as the critical point (green point). The saturation pressures P_{sat} predicted by the vdW and RK EoS were compared with the experimental values obtained from the NIST data (black points) [38]. Moreover, the predicted superheat limit temperature T_{sp} at the atmospheric pressure (358.2 K by vdW EoS and 378.8 K by RK EoS) were also compared with the experimental measurement (381.5 K [44], pink point). It is obvious that the P_{sat} and T_{sp} predicted by the RK EoS are more accurate than the ones predicted by the vdW EoS owning to a better agreement of both P_{sat} and T_{sp} with experimental results. Therefore, the superior RK EoS was eventually selected to predict the phase-change thermodynamics of the PFP over a wide range of the liquid state, metastable state, and vapor state for a higher accuracy.

Based on the predicted phase diagram, a schematic diagram displaying the procedures of ADV nucleation occurring in a metastable PFP nanodroplet under ultrasound stimulation was illustrated in Fig. 4(b). The dashed arrow depicts the isothermal depressurization path at the physiological temperature (310 K) throughout the entire procedures (A → D). At the initial thermodynamic state (point A), the PFP nanodroplet is stable as long as its initial internal pressure P_{l0} is larger than the saturation pressure P_{sat} (point B), where the liquid is in equilibrium with its vapor. Note that the P_{l0} is generally larger than the P_{sat} due to the PFP nanodroplet always experiences a relatively high Laplace pressure P_{Lap}. With the liquid pressure P_l in the PFP nanodroplet decreasing due to the negative ultrasound pressures P_a, the PFP liquid enters a metastable state as $P_l < P_{sat}$, and it would be remained until the ADV nucleation occurs (point C) in the metastable liquid, which is accurately described by the modified CNT. Once the depressurization reaching the spinodal pressure P_{spin} (point D, −5.26 MPa obtained from the RK EoS), liquid-to-vapor phase change occurs spontaneously due to spinodal decomposition [45].

3.2. Description of ADV nucleation in a PFP nanodroplet

Fig. 5 showed the predicted (a) critical work W^*, (b) critical radius r^* and (c) nucleation rate J of the ADV nucleation events occurred in a PFP nanodroplet versus varying ultrasound amplitude P_A using the CNT and the modified CNT with/without the Laplace pressure effect. When the P_A increases, the scaled overpressure ξ increases, resulting in much smaller critical work and critical radii, but larger nucleation rates. Both CNT and modified CNT have similar variation tendencies, that is, the ADV nucleation is facilitated by the ultrasound with larger amplitudes. However, the closer to the spinodal point ($\xi = 1$) the thermodynamic condition is, the larger difference between the CNT and the modified CNT will be. Near saturation condition ($\xi = 0$), the CNT is expected to provide accurate results, whereas its predictions become increasingly inaccurate as the thermodynamic condition is approaching to the spinodal point [33]. At the spinodal, the critical work and critical radius predicted by the CNT are larger than zero, as an indication of the intrinsic limitations of the CNT. By contrast, the corresponding values predicted by the modified CNT become zero, in accordance with the fact that the critical work disappears at the spinodal and spinodal

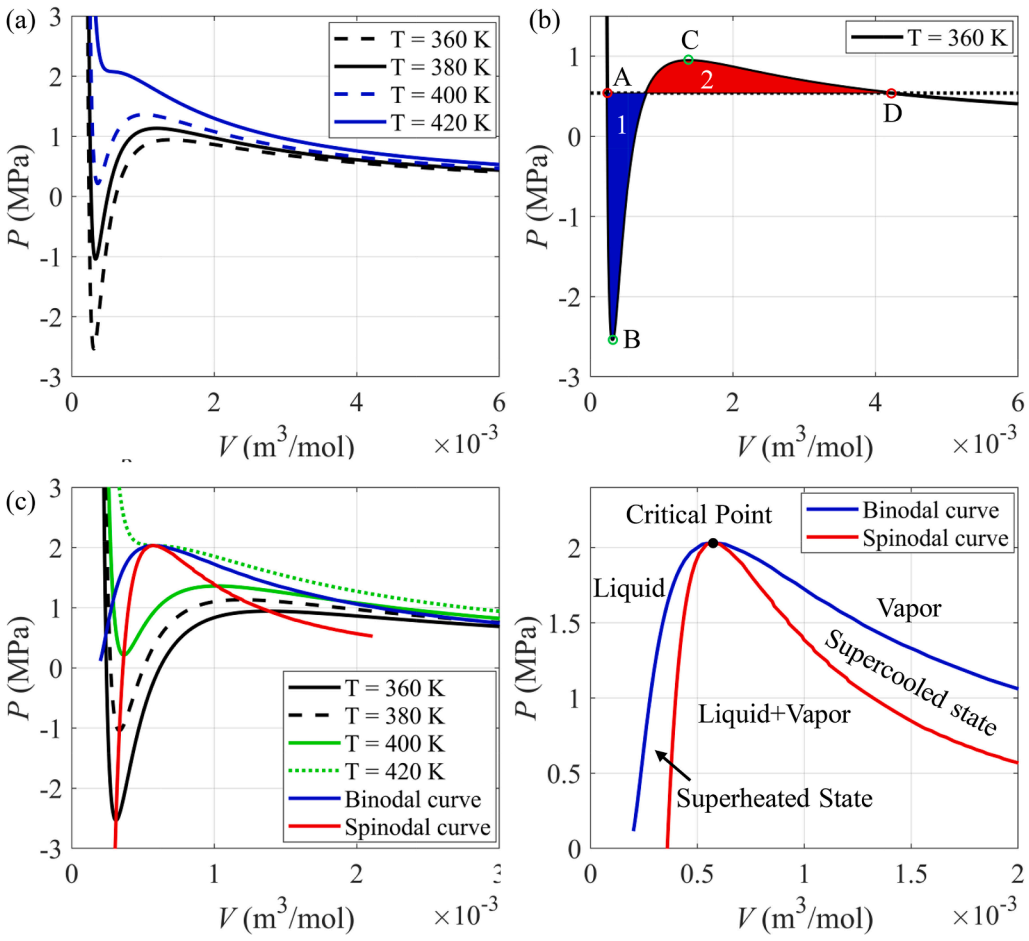

Fig. 3. Phase-change thermodynamics of the PFP determined by the Redlich-Kwong cubic equation of state. (a) Isotherms showing the relationship between pressure and volume for 4 different temperatures. (b) Plot showing the isobaric line at an isotherm for a liquid–vapor equilibrium. The areas of regions 1 and 2 are equivalent and it is the so-called Maxwell's construction. (c) Construction of the binodal (saturation) curve and spinodal curve based on the isothermal pressure–volume curves. (d) A pressure–volume phase diagram of the PFP.

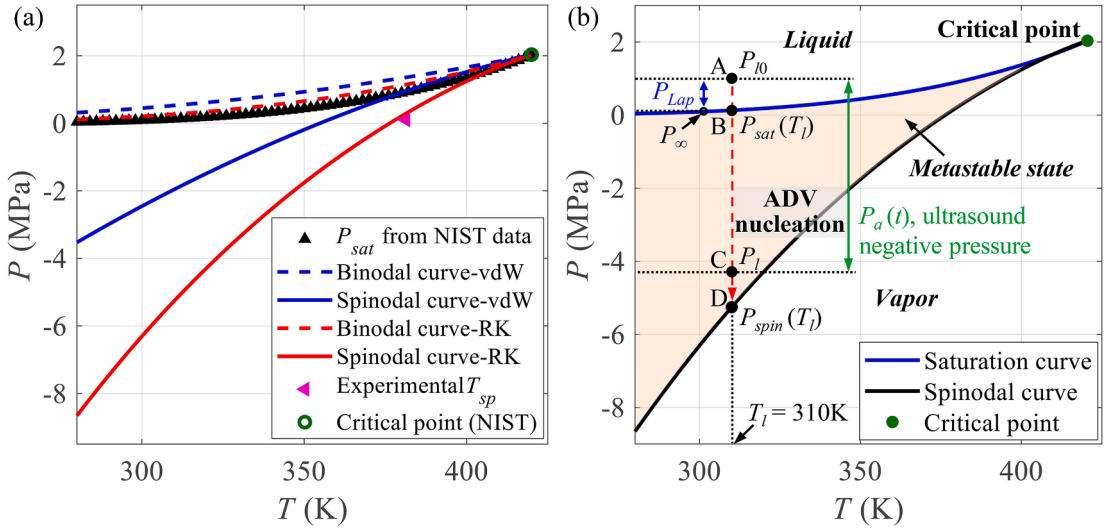

Fig. 4. (a) The pressure–temperature phase diagram of PFP predicted by the van der Waals (vdW) and the Redlich–Kwong (RK) equations of state. The experimental values of saturation pressure P_{sat} (black points) and superheated limit temperature T_{sp} (pink point) were obtained from the NIST data [38] and Ref. [44], respectively. (b) Phase diagram to describe the procedures of ADV nucleation that occurs in a metastable PFP nanodroplet (A → D). The metastable liquid state is bounded by the spinodal and binodal (saturation) curves, which meet in at the critical point (green point). (For interpretation of the references to colour in this figure legend, the reader is referred to the web version of this article.)

decomposition takes place spontaneously [45]. This discrepancy exemplified the intrinsic limitations of the CNT in the description of microscopic ADV nucleation events, especially for larger negative acoustic pressures; meanwhile, it also highlighted the necessity to modify the CNT and the superiority of the modified CNT while dealing with the microscopic ADV nucleation. Moreover, note that the Laplace pressure P_{Lap} increases the value of P_l according to Eq. (3), and thereby increases the critical radius and reduces the nucleation rate, suggesting

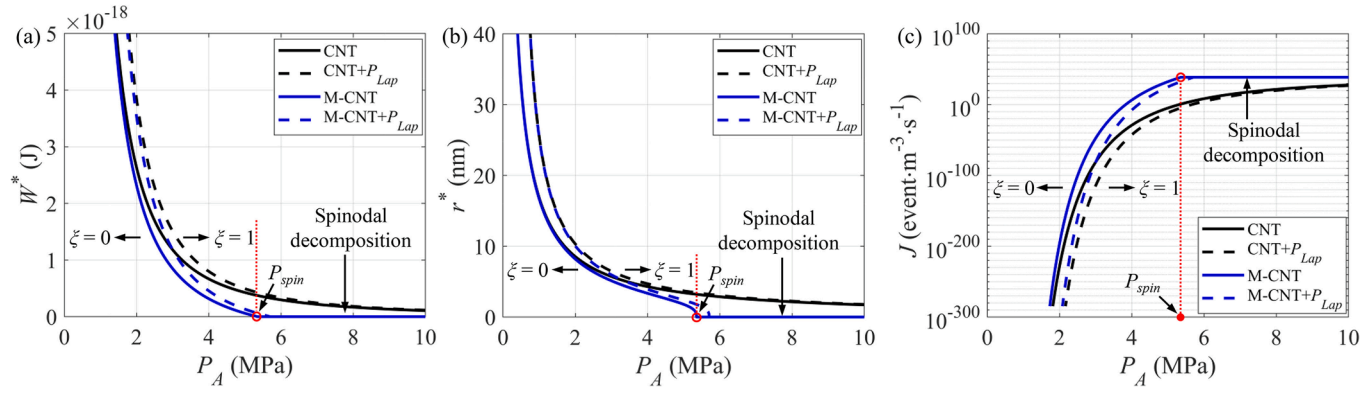

Fig. 5. Comparison of the ADV nucleation occurring in PFP nanodroplets predicted by the CNT and the modified CNT with/without the Laplace pressure effect. (a) The critical work W^*, (b) critical radius r^* and (c) nucleation rate J of the ADV nucleation subjected to ultrasound with different amplitudes P_A. The experimentally controllable scaled overpressure of liquid phase ξ ranges from 0 at the binodal (phase coexistence) to 1 at the spinodal.

that the Laplace pressure is an important factor adversely to the occurrence of ADV nucleation in a PFP nanodroplet. This may also contribute to the experimentally observed *in vivo* stability of superheated PFP nanodroplets against spontaneous vaporization.

3.3. ADV nucleation thresholds of PFP nanodroplets

Under ultrasound stimulation with varying amplitudes, the probabilities of ADV nucleation Σ predicted by the CNT and the modified CNT with/without the Laplace pressure effect were presented in Fig. 6(a). Introducing Σ = 50% as a criterion, the CNT predicted a much larger ADV nucleation threshold P_{th} (8.98 MPa) than that predicted by the modified CNT (4.55 MPa) taking the Laplace pressure effect into account, as displayed by the points in Fig. 6(a). The great difference in the predicted ADV nucleation thresholds can be explained that the CNT predicts a reduced nucleation rate because of its intrinsic limitations (Fig. 5(c)) and consequently might lead to an obvious overestimation of ADV nucleation threshold, especially for larger negative acoustic pressures. Note that the Laplace pressure obviously increased the ADV nucleation thresholds of the PFP nanodroplets, indicating the necessity to consider the effect of Laplace pressure on the ADV nucleation. Furthermore, the P_{th} at different liquid temperatures T_l were predicted by the CNT and the modified CNT, and the liquid pressure thresholds of ADV nucleation P_l^N were calculated according to Eqs. (3) and (14), as shown in Fig. 6(b). All values predicted by the CNT are much smaller than those predicted by the modified CNT. It should be noted that the P_l^N predicted by the CNT are far below the corresponding spinodal pressures $P_{spin}(T_l)$ at all temperatures, whereas all values predicted by the modified CNT are larger than the corresponding $P_{spin}(T_l)$. As shown in Fig. 4 (b), spinodal decomposition takes place spontaneously when the liquid pressure P_l is decreased to the P_{spin} [45], thus the predictions of P_l^N by the CNT that are below the P_{spin} should be deemed invalid. These results give further verification that the modified CNT is more accurate and preferable for predicting the ADV nucleation threshold of PFP nanodroplets.

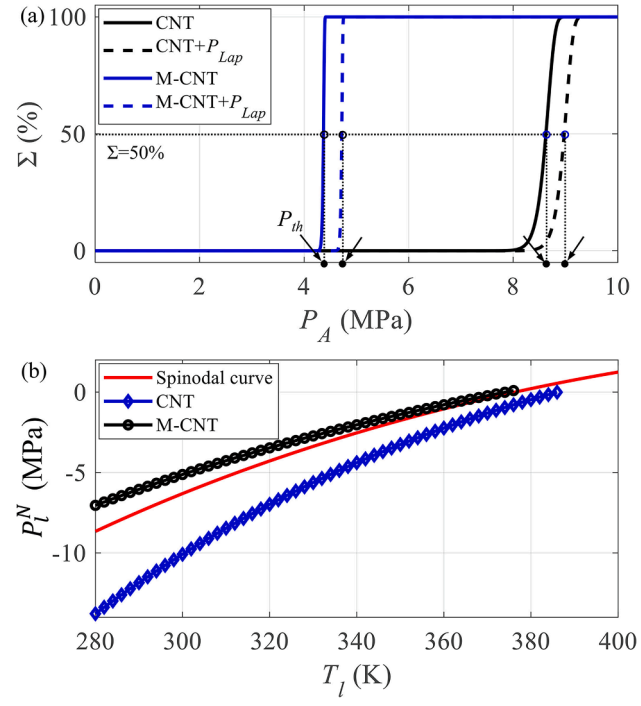

Fig. 6. The ADV nucleation thresholds of PFP nanodroplets predicted by the CNT and the modified CNT with/without the Laplace pressure effect at a fixed temperature (T_l = 310 K). (a) Nucleation probability Σ as a function of ultrasound amplitude P_A. (b) The calculated liquid pressure thresholds of ADV nucleation P_l^N with the CNT and the modified CNT at different temperatures T_l.

3.4. Effects of droplet properties on ADV nucleation thresholds

The effects of droplet radius R_d and surface tension at the droplet-water interface σ_{dw} on the ADV nucleation of PFP nanodroplets were presented in Fig. 7. With ultrasound amplitude P_A increasing, the mappings of nucleation probability Σ at different R_d and σ_{dw} were plotted in Fig. 7(a) and (b), respectively. It showed that the Σ gradually increases with an increase in the P_A or R_d (or both), while it decreases as the σ_{dw} increases. Consequently, the predicted ADV nucleation threshold P_{th} decreases with the R_d increasing and σ_{dw} decreasing as shown in Fig. 7(c) and (d), exhibiting much stronger influences for smaller nanodroplets. This dependence can be attributed to the effect of Laplace pressure P_{Lap} on the nanodroplets. The σ_{dw} for 'naked' (i.e., without coating) PFP nanodroplets is 56 ± 1 mN m^{-1} [46], and it would be significantly reduced by coating a shell with lipid, surfactant, albumin, or polymer [2]. The predictions of P_{th} with reduced σ_{dw} = 14 mN m^{-1} and σ_{dw} = 32 mN m^{-1} agree well with the experimental ADV thresholds of PFP nanodroplets coated by lipids (red point), fluorinated surfactant (Zonyl FSO, blue point) and polymer (PLGA, black point) shells, respectively [18].

According to Eq. (4), the Laplace pressure P_{Lap} is inversely proportional to droplet radius R_d and directly proportional to surface tension σ_{dw}, so that the initial liquid pressure P_{l0} in the PFP nanodroplet is larger for a smaller nanodroplet that is more stable against droplet vaporization, as shown in Fig. 8(a). The presence of a shell reduces the surface tension σ_{dw} and the experienced P_{Lap} of the nanodroplet, resulting in a linear decrease in the P_{th} as summarized from 76 nanodroplets with

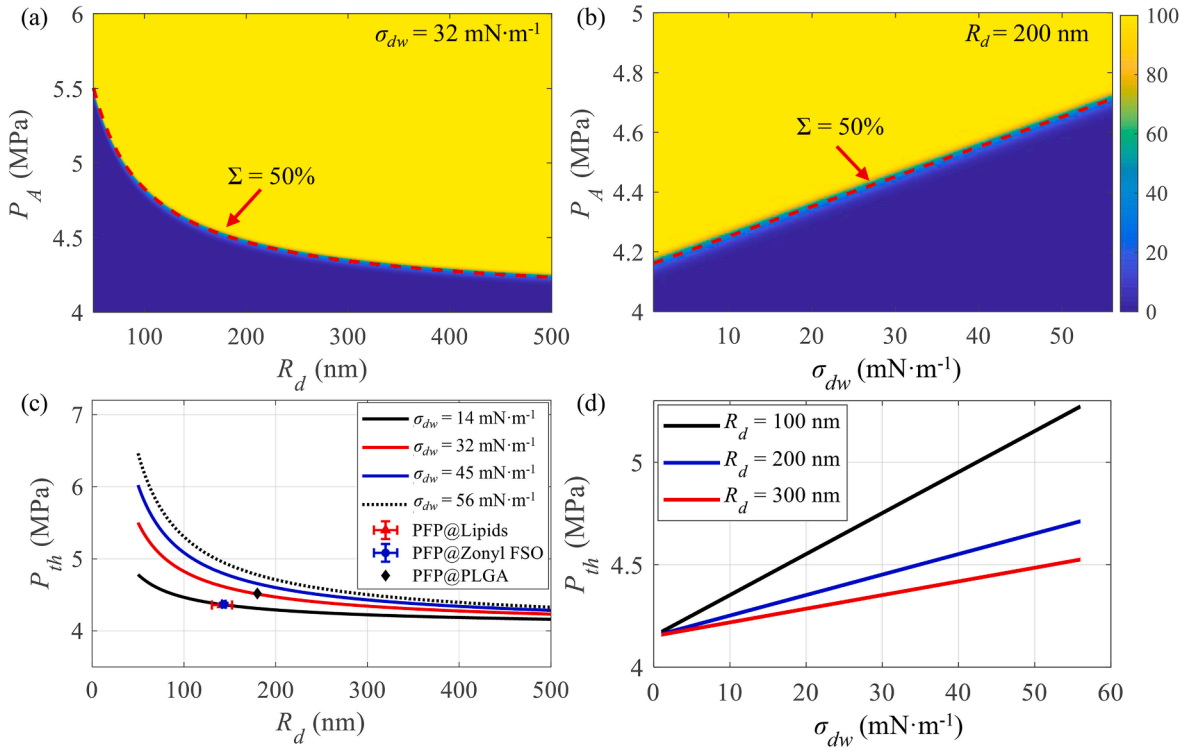

Fig. 7. The effects of droplet radius R_d and surface tension σ_{dw} on the ADV nucleation threshold of PFP nanodroplets. (a) The mapping of nucleation probability Σ at different P_A and R_d, while (b) representing that at different P_A and σ_{dw}. (c) and (d) representing the predicted nucleation thresholds P_{th} as a function of R_d and σ_{dw}, respectively. In the figure (c), the points with bar represent the experimental measurements [18].

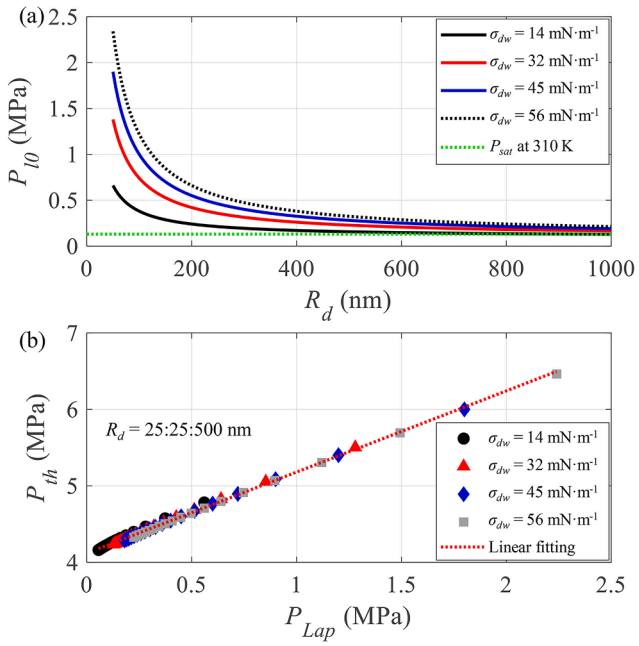

Fig. 8. (a) The initial liquid pressure P_{l0} in the PFP nanodroplets with different droplet radius R_d and surface tension σ_{dw} taking into account the Laplace pressure effect. (b) The relationship between the predicted ADV nucleation thresholds P_{th} and the Laplace pressures P_{Lap} summarized from 76 different PFP nanodroplets.

different R_d and σ_{dw} as shown in Fig. 8(b). Encapsulating the nanodroplet in a shell (e.g., lipids/fluorinated surfactant) not only stabilizes them from coalescence, but also leads to a lower surface tension and a significant decrease in ADV nucleation threshold, which could act as a practical strategy to achieve an optimal balance between the *in vivo* stability and the ADV threshold of the PFC nanodroplet.

3.5. *Effects of acoustic parameters on ADV nucleation thresholds*

The effects of ultrasound frequency f and pulse duration τ_p on the ADV nucleation threshold P_{th} of the PFP nanodroplets with different radius R_d were further investigated as presented in Fig. 9. The ADV nucleation threshold slightly increases with the ultrasound frequency increasing, while it slightly decreases with the ultrasound pulse duration increasing. The decreasing trend of the ADV nucleation threshold with decreasing frequency and/or increasing pulse duration can be explained that the nanodroplets experience a longer duration of negative acoustic pressure at lower frequency and/or longer pulse duration, which in turn increases the probability of ADV nucleation and consequently decreases the ADV nucleation threshold. Such weak dependence agrees well with previous studies that using the CNT to describe the ADV nucleation of the PFP microdroplets [29,30]. Moreover, a similar variation tendency has also been observed in previous experiments, but the experimentally measured ADV threshold shows a stronger dependence on the ultrasound frequency as compared to the ADV nucleation threshold [15,16]. It can be explained that the ultrasound pulse with lower frequency or longer pulse duration would also provide a longer time window for growth of the nano-sized bubble nuclei ($r^* < 10$ nm according to Fig. 5 (b)), making them easier to be detected experimentally. In addition, numerical investigations have also demonstrated that the ADV threshold determined by the bubble growth behavior obviously increases with the ultrasound frequency increasing [27,28], which is consistent with the experimental data for ADV threshold [15,16].

4. Conclusions

A modified CNT was developed for describing the initial ADV nucleation that occurs in a metastable PFP nanodroplet by utilizing the

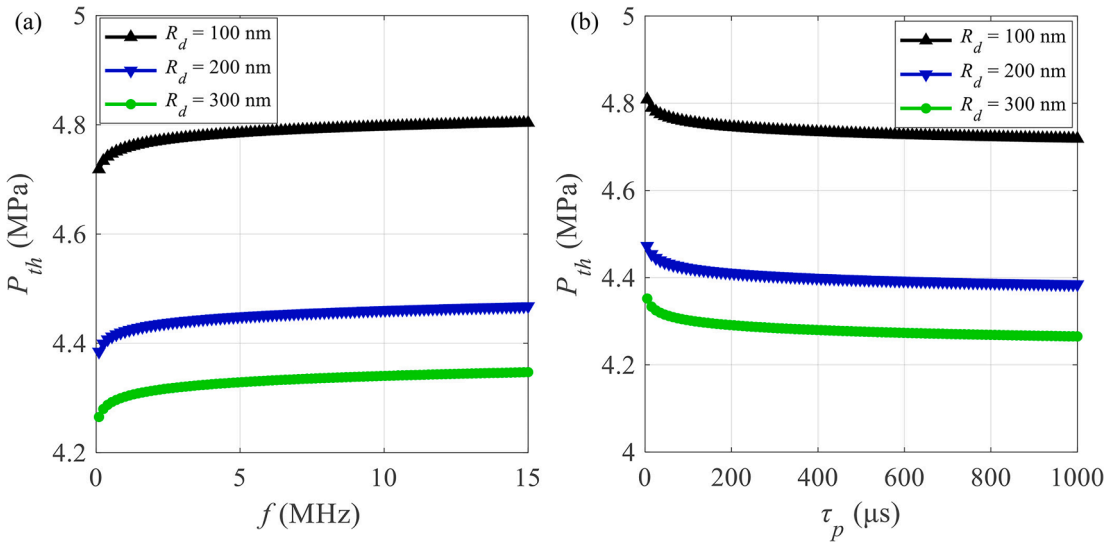

Fig. 9. The effects of (a) ultrasound frequency f and (b) pulse duration τ_p on the ADV nucleation threshold of PFP nanodroplets (T_l = 310 K).

surface tension $\sigma_r(\xi)$ instead of the σ_∞, and meanwhile considering the Laplace pressure effect. The scaled overpressure ξ is determined by the actual pressure and temperature in the PFP nanodroplet, as well as its phase-change thermodynamics that can be accurately predicted by the cubic RK EoS rather than the vdW EoS. Compared to the CNT, the modified CNT could overcome the intrinsic limitations of the CNT, and it predicted a larger nucleation rate and a lower ADV nucleation threshold, which agree much better with experimental results. Furthermore, the predicted ADV nucleation thresholds of the PFP nanodroplets increase considerably as the droplet radius decreases and the surface tension at the droplet-water interface increases, especially for smaller nanodroplets. The presence of a stabilizing shell reduces the effective surface tension at the droplet-water interface and consequently reduces the ADV nucleation threshold, providing a practical strategy for optimal balance of *in vivo* stability and ADV threshold. In contrast, ultrasound frequency and pulse duration both have little effects on the ADV nucleation threshold. This study may contribute to further understanding ADV mechanisms for PFC nanodroplet and promoting its potential theranostic applications *in vivo*.

CRediT authorship contribution statement

Dui Qin: Conceptualization, Methodology, Writing - original draft, Writing - review & editing, Funding acquisition. **Qingqin Zou:** Software, Validation, Visualization. **Shuang Lei:** Software, Validation. **Wei Wang:** Writing - review & editing. **Zhangyong Li:** Conceptualization, Project administration, Supervision, Resources, Writing - review & editing.

Declaration of Competing Interest

The authors declare that they have no known competing financial interests or personal relationships that could have appeared to influence the work reported in this paper.

Acknowledgements

This work was supported by the National Natural Science Foundation of China (Grant No. 11904042), the Natural Science Foundation of Chongqing, China (Grant No. cstc2019jcyj-msxmX0534), and the Science and Technology Research Program of Chongqing Municipal Education Commission (Grant No. KJQN202000617).

References

[1] A.L.Y. Kee, B.M. Teo, Biomedical applications of acoustically responsive phase shift nanodroplets: Current status and future directions, Ultrason. Sonochem. 56 (2019) 37–45.
[2] H. Lea-Banks, M.A. O'Reilly, K. Hynynen, Ultrasound-responsive droplets for therapy: A review, J. Control. Release 293 (2019) 144–154.
[3] K. Loskutova, D. Grishenkov, M. Ghorbani, Review on acoustic droplet vaporization in ultrasound diagnostics and therapeutics, Biomed Res. Int. 2019 (2019) 1–20.
[4] M.A. Borden, G. Shakya, A. Upadhyay, K.-H. Song, Acoustic nanodrops for biomedical applications, Curr. Opin. Colloid Interface Sci. 50 (2020) 101383, https://doi.org/10.1016/j.cocis.2020.08.008.
[5] B.L. Helfield, K. Yoo, J. Liu, R. Williams, P.S. Sheeran, D.E. Goertz, P.N. Burns, Investigating the accumulation of submicron phase-change droplets in tumors, Ultrasound Med. Biol. 46 (10) (2020) 2861–2870.
[6] T.O. Matsunaga, P.S. Sheeran, S. Luois, J.E. Streeter, L.B. Mullin, B. Banerjee, P. A. Dayton, Phase-change nanoparticles using highly volatile perfluorocarbons: toward a platform for extravascular ultrasound imaging, Theranostics 2 (12) (2012) 1185–1198.
[7] R. Williams, C. Wright, E. Cherin, N. Reznik, M. Lee, I. Gorelikov, F.S. Foster, N. Matsuura, P.N. Burns, Characterization of submicron phase-change perfluorocarbon droplets for extravascular ultrasound imaging of cancer, Ultrasound Med. Biol. 39 (3) (2013) 475–489.
[8] N. Rapoport, K.-H. Nam, R. Gupta, Z. Gao, P. Mohan, A. Payne, N. Todd, X. Liu, T. Kim, J. Shea, C. Scaife, D.L. Parker, E.-K. Jeong, A.M. Kennedy, Ultrasound-mediated tumor imaging and nanotherapy using drug loaded, block copolymer stabilized perfluorocarbon nanoemulsions, J. Control. Release 153 (1) (2011) 4–15.
[9] J. Liu, F. Xu, J.u. Huang, J. Xu, Y. Liu, Y. Yao, M. Ao, A.o. Li, L. Hao, Y. Cao, Z. Hu, H. Ran, Z. Wang, P. Li, Low-intensity focused ultrasound (LIFU)-activated nanodroplets as a theranostic agent for noninvasive cancer molecular imaging and drug delivery, Biomater. Sci. 6 (11) (2018) 2838–2849.
[10] C.-H. Fan, Y.-T. Lin, Y.-J. Ho, C.-K. Yeh, Spatial-temporal cellular bioeffects from acoustic droplet vaporization, Theranostics 8 (20) (2018) 5731–5743.
[11] D. Qin, L. Zhang, N. Chang, P. Ni, Y. Zong, A. Bouakaz, M. Wan, Y.i. Feng, In situ observation of single cell response to acoustic droplet vaporization: Membrane deformation, permeabilization, and blebbing, Ultrason. Sonochem. 47 (2018) 141–150.
[12] P. Zhang, T. Porter, An in vitro study of a phase-shift nanoemulsion: a potential nucleation agent for bubble-enhanced HIFU tumor ablation, Ultrasound Med. Biol. 36 (2010) 1856–1866.
[13] L.C. Moyer, K.F. Timbie, P.S. Sheeran, R.J. Price, G.W. Miller, P.A. Dayton, High-intensity focused ultrasound ablation enhancement in vivo via phase-shift nanodroplets compared to microbubbles, J. Ther. Ultrasound 3 (2015) 1–9.
[14] H. Lea-Banks, Y. Meng, S.K. Wu, R. Belhadjhamida, C. Hamani, K. Hynynen, Ultrasound-sensitive nanodroplets achieve targeted neuromodulation, J. Control. Release 332 (2021) 30–39.
[15] M. Aliabouzar, K.N. Kumar, K. Sarkar, Acoustic vaporization threshold of lipid-coated perfluoropentane droplets, J. Acoust. Soc. Am. 143 (2018) 2001–2012.
[16] M. Aliabouzar, K.N. Kumar, K. Sarkar, Effects of droplet size and perfluorocarbon boiling point on the frequency dependence of acoustic vaporization threshold, J. Acoust. Soc. Am. 145 (2019) 1105–1116.
[17] S. Raut, M. Khairalseed, A. Honari, S.R. Sirsi, K. Hoyt, Impact of hydrostatic pressure on phase-change contrast agent activation by pulsed ultrasound, J. Acoust. Soc. Am. 145 (2019) 3457–3466.

[18] R. Melich, P. Bussat, L. Morici, A. Vivien, E. Gaud, T. Bettinger, S. Cherkaoui, Microfluidic preparation of various perfluorocarbon nanodroplets: characterization and determination of acoustic droplet vaporization (ADV) threshold, Int. J. Pharm. 587 (2020), 119651.
[19] Q. Wu, C. Mannaris, J.P. May, L. Bau, A. Polydorou, S. Ferri, D. Carugo, N.D. Evans, E. Stride, Investigation of the acoustic vaporization threshold of lipid-coated perfluorobutane nanodroplets using both high-speed optical imaging and acoustic methods, Ultrasound Med. Biol. (2021) in press.
[20] P.S. Sheeran, S.H. Luois, L.B. Mullin, T.O. Matsunaga, P.A. Dayton, Design of ultrasonically-activatable nanoparticles using low boiling point perfluorocarbons, Biomaterials 33 (2012) 3262–3269.
[21] J.D. Rojas, P.A. Dayton, Vaporization detection imaging: A technique for imaging low-boiling-point phase-change contrast agents with a high depth of penetration and contrast-to-tissue ratio, Ultrasound Med. Biol. 45 (2019) 192–207.
[22] A. Kabalnov, D. Klein, T. Pelura, E. Schutt, J. Weers, Dissolution of multicomponent microbubbles in the bloodstream: 1. Theory, Ultrasound Med. Biol. 24 (5) (1998) 739–749.
[23] P.A. Mountford, M.A. Borden, On the thermodynamics and kinetics of superheated fluorocarbon phase-change agents, Adv. Colloid Interface Sci. 237 (2016) 15–27.
[24] T. Abbasi, S. Abbasi, Accidental risk of superheated liquids and a framework for predicting the superheat limit, J. Loss Prev. Process Ind. 20 (2007) 165–181.
[25] M. Guédra, F. Coulouvrat, A model for acoustic vaporization of encapsulated droplets, J. Acoust. Soc. Am. 138 (2015) 3656–3667.
[26] T. Lacour, M. Guédra, T. Valier-Brasier, F. Coulouvrat, A model for acoustic vaporization dynamics of a bubble/droplet system encapsulated within a hyperelastic shell, J. Acoust. Soc. Am. 143 (2018) 23–37.
[27] T. Lacour, T. Valier-Brasier, F. Coulouvrat, Ultimate fate of a dynamical bubble/droplet system following acoustic vaporization, Phys. Fluids 32 (2020), 051702.
[28] S. Park, G. Son, Numerical investigation of acoustic vaporization threshold of microdroplets, Ultrason. Sonochem. 71 (2021), 105361.
[29] M. Aliabouzar, O.D. Kripfgans, W.Y. Wang, B.M. Baker, J. Brian Fowlkes, M. L. Fabiilli, Stable and transient bubble formation in acoustically-responsive scaffolds by acoustic droplet vaporization: theory and application in sequential release, Ultrason. Sonochem. 72 (2021) 105430, https://doi.org/10.1016/j.ultsonch.2020.105430.
[30] C.J. Miles, C.R. Doering, O.D. Kripfgans, Nucleation pressure threshold in acoustic droplet vaporization, J. Appl. Phys. 120 (2016), 034903.
[31] V.I. Kalikmanov, Classical nucleation theory, Springer, 2013.
[32] M.E.M. Azouzi, C. Ramboz, J.F. Lenain, F. Caupin, A coherent picture of water at extreme negative pressure, Nat. Phys. 9 (2013) 38–41.
[33] M.O. de Andrade, S.R. Haqshenas, K.J. Pahk, N. Saffari, The effects of ultrasound pressure and temperature fields in millisecond bubble nucleation, Ultrason. Sonochem. 55 (2019) 262–272.
[34] D. Kashchiev, Determining the curvature dependence of surface tension, J. Chem. Phys. 118 (20) (2003) 9081–9083.
[35] D. Qin, Y.i. Feng, M. Wan, Modeling photoacoustic cavitation nucleation and bubble dynamics with modified classical nucleation theory, J. Acoust. Soc. Am. 138 (3) (2015) 1282–1289.
[36] D. Kashchiev, Nucleation work, surface tension, and Gibbs-Tolman length for nucleus of any size, J. Chem. Phys. 153 (12) (2020) 124509, https://doi.org/10.1063/5.0021337.
[37] B.E. Poling, J.M. Prausnitz, J.P. O'connell, Properties of gases and liquids, McGraw-Hill Education, 2001.
[38] NIST, Thermophysical properties of fluid systems, in, Database, 2018.
[39] C.F. Delale, Jan Hruby, F. Marsik, Homogeneous bubble nucleation in liquids: The classical theory revisited, J. Chem. Phys. 118 (2) (2003) 792–806.
[40] H.J. Maris, Introduction to the physics of nucleation, C. R. Phys. 7 (9-10) (2006) 946–958.
[41] A. Dias, F. Llovell, J. Coutinho, I. Marrucho, L. Vega, Thermodynamic characterization of pure perfluoroalkanes, including interfacial and second order derivative properties, using the crossover soft-SAFT EoS, Fluid Phase Equilib. 286 (2009) 134–143.
[42] A. Dias, A. Caço, J. Coutinho, L. Santos, M. Pineiro, L. Vega, M.C. Gomes, I. Marrucho, Thermodynamic properties of perfluoro-n-octane, Fluid Phase Equilib. 225 (2004) 39–47.
[43] G.J. Zarragoicoechea, V.A. Kuz, van der Waals equation of state for a fluid in a nanopore, Phys. Rev. E 65 (2002), 021110.
[44] M. Blander, J.L. Katz, Bubble nucleation in liquids, AIChE J. 21 (1975) 833–848.
[45] M. Hillert, Phase equilibria, phase diagrams and phase transformations: their thermodynamic basis, Cambridge University Press, 2007.
[46] L.Y. Clasohm, I.U. Vakarelski, R.R. Dagastine, D.Y. Chan, G.W. Stevens, F. Grieser, Anomalous pH dependent stability behavior of surfactant-free nonpolar oil drops in aqueous electrolyte solutions, Langmuir 23 (2007) 9335–9340.